PERGAMON

Journal of Structural Geology 22 (2000) 25–42

JOURNAL OF STRUCTURAL GEOLOGY

www.elsevier.nl/locate/jstrugeo

Sequential growth of deformation bands in the laboratory

Karen Mair [1], Ian Main, Stephen Elphick

Department of Geology and Geophysics, University of Edinburgh, West Mains Road, Edinburgh EH9 3JW, UK

Received 26 January 1999; accepted 24 June 1999

Abstract

We investigate the formation and evolution of localised faulting in high porosity sandstone by laboratory triaxial compression of intact 100-mm-diameter core samples. Experiments were carried out dry, at constant confining pressure (34 MPa), constant axial strain rate (5×10^{-6} s^{-1}) and increasing axial strain (1.5–11.2%). Tests generated fault zones consisting of sets of distinct pale granulated strands, separated by lenses of apparently undamaged host rock. The sets of strands were sub-parallel to the shear direction but showed complex anastamosing geometry in perpendicular section. The individual strands had reduced grain size, porosity and sorting compared to undeformed rock. A strong correlation was found between the number of strands occurring in a fault zone and the applied axial strain. Mean grain size, however, reached a steady value irrespective of axial strain. This implies that a limited amount of strain is accommodated on each strand with further strain requiring new strands to form. However, no direct evidence for strain hardening was observed in the post-failure macroscopic stress–strain curves. Our laboratory induced deformation zones strongly resemble the key characteristics of natural deformation bands. We show the first laboratory evidence for the sequential development of increasing numbers of discrete deformation bands with increasing strain.

1. Introduction

In this paper we present new experimental results showing the sequential development of cataclastic faults in a high porosity sandstone. The motivation for this work is to examine the mechanical and hydraulic properties of porous rocks during deformation. These properties depend on the microstructural evolution of the rock, in particular, the micromechanical processes which have acted during fault formation, how these processes have interacted, and what stage of evolution has been reached. We present a brief review of previous studies focusing on the characteristics of the faults observed in the field and deformation mechanisms which are consistent with these observations. We then show how our new laboratory studies may improve understanding of fault development in porous sandstone.

Faults occurring in highly porous, quartz-rich sandstone units have been studied in several field areas. They have been referred to in the literature as 'deformation bands' (Aydin, 1978; Aydin and Johnson, 1978), 'microfaults' (Jamison and Stearns, 1982), 'granulation seams' (Pittman, 1981), and simply 'faults' (Underhill and Woodcock, 1987). We adopt the terminology of Aydin and co-workers throughout this paper.

These studies have shown that faulting in highly porous, quartz-rich sandstone is typically expressed as a complex zone consisting of sets of distinct pale deformation bands (observable on hand specimen scale). They form an anastamosing web of damage, and are separated by lenses of apparently undamaged host rock (e.g. Aydin and Johnson, 1978). In the plane parallel to the direction of shear, these same deformation bands have approximately straight traces which lie sub-parallel to the shearing direction (e.g. Aydin and Johnson, 1978). These damage zones are often more resistant to weathering allowing easy identification in

E-mail address: karen@barre.mit.edu (K. Mair).

[1] Now at: Department of Earth, Atmospheric and Planetary Sciences, Massachusetts Institute of Technology, Cambridge, MA 02139, USA.

0191-8141/00/$ - see front matter
PII: S0191-8141(99)00124-8

the field. The individual deformation bands are discrete zones of intense cataclasis, a few millimetres wide which accommodate small offsets, and have the mineralogy of the host rock. They are sites of concentrated damage where grain size, the degree of sorting, and porosity are all reduced with respect to the host rock.

Aydin and Johnson (1983) categorised the features in terms of displacement measured from bedding offsets: (i) single *deformation bands* have millimetre-scale offset; (ii) *zones of deformation bands* occur as a series of distinct bands and accumulate centimetre- to decimetre-scale offsets; (iii) *slip surfaces* are localised onto a single plane and accommodate metres of offset. The individual deformation band units occur both as isolated bands and in zones. In contrast, however, slip surfaces are always closely associated with zones of deformation bands and never occur independently (Aydin, 1978; Aydin and Johnson, 1978). From these field observations of spatial relationships, Aydin and Johnson (1983) proposed that deformation bands develop sequentially as follows: (i) the initial band causes a very small offset; (ii) two bands cause a greater offset; (iii) a *zone of bands* develop causing significant offset; (iv) deformation then localises onto a single *slip surface* which accommodates much greater displacement. This model is consistent with most field observations (e.g. Jamison and Stearns, 1982; Underhill and Woodcock, 1987; Antonellini et al., 1994). However, the proposed sequential development of deformation bands associated with progressive offset has never been observed under laboratory conditions. Accordingly, one of the prime aims of our study is to test this hypothesis in the laboratory.

This study focuses on *cataclastic* deformation bands, formed in quartz-rich, high porosity sandstone. They are characterised by reductions in grain size, sorting, pore space and an increase in grain angularity, which are all consistent with a cataclastic granulation mechanism (Underhill and Woodcock, 1987). It is important to be aware that other types of deformation bands (e.g. dilatant bands, compaction bands, clay smear bands) do occur (Antonellini et al., 1994). The structural characteristics and the mere existence of such deformation bands are strongly dependent on the initial composition and porosity of the host rock in addition to the stress environment.

The observations of multiple, closely spaced subparallel bands which each have limited displacement, suggests that deformation shifts between bands in order to accommodate bulk strain. The mechanism generally envisaged to promote this behaviour is strain (work) hardening, possibly caused by increased grain contact friction in the bands (Jamison and Stearns, 1982; Aydin and Johnson, 1983; Underhill and Woodcock, 1987; Fowles and Burley, 1994). Strain hardening on the band would encourage subsequent deformation to localise in the virgin host rock rather than continue to slip along a pre-existing, but now stronger, fault. This process could result in bulk deformation accommodated across a distributed zone of parallel bands.

In contrast, slip surfaces have straight traces, striations and grooves, and accommodate large strain along a single plane. These very different characteristics imply a strain softening mechanism of formation (Aydin, 1978; Jamison and Stearns, 1982; Underhill and Woodcock, 1987) similar to that inferred for most brittle faults. Therefore, the active deformation mechanism proposed for the growth of zones of deformation bands (i.e. strain hardening) is different to that invoked for slip surface development (i.e. strain softening). The transition from zones of deformation bands to slip surfaces is not well understood, however Aydin and Johnson (1983), following the theories of Rudnicki and Rice (1975), propose that the deformation bands are stiffer (due to grain crushing and consolidation) and further deformation becomes easier outside the fault zone in the softer matrix, hence slip surfaces can develop there.

Hirth and Tullis (1989) observed, in their experiments on quartzite, that cataclastic flow was a transient strain hardening phenomenon that only lasted while pores were collapsing. At high strains they found shear localisation replaced cataclastic flow as the dominant deformation style. If deformation bands are regarded as a form of cataclastic flow which is replaced by shear localisation at high strains, this laboratory observation may offer an explanation for the switch from the formation of zones of deformation bands to deformation localised on slip surfaces.

The mechanisms responsible for the development of deformation bands are uncertain, however it is clear that each new deformation episode is strongly influenced by the history of the rock, implying that the mechanical characteristics of a rock are a function of total strain and the type of damage sustained during deformation (Jamison and Stearns, 1982). As a consequence, one of the main objectives of the work presented here is to examine the effect of increasing strain.

Previous laboratory experiments have produced features which exhibit many of the characteristics of natural faults, e.g. Dunn et al. (1973), Friedman and Logan (1973), Engelder (1974). They have offered good explanations to certain stages of the faulting process, in particular the formation of a single deformation band. However, to the authors' knowledge, no previous experiments have reproduced geologically realistic faults showing the hierarchical development of sets of deformation bands side by side. This may be due in part to the limited size of cylindrical samples (25.4–38.1 mm diameter) generally used in previous ex-

Table 1
Locharbriggs sandstone characterisation[a]

Description	Locharbriggs Sandstone: Lower Permian, Aeolian Sandstone
Initial grain size	fine–medium (200 μm)
Grain shape	rounded–well rounded
Cement	hematite (and some silica)
Porosity	22.2%
Semi-quantitative modal mineralogy (%) using XRD	
Quartz	88.1%
K-Feldspar	5.9%
Kaolinite	0.0%
Siderite	0.0%
Dolomite	0.0%
Major element (%) using XRF	
SiO_2	95.2%
Al_2O_3	2.6%
FeO	0.5%
MgO	0.1%
Na_2O	0.0%
K_2O	1.5%
TiO_2	0.1%
MnO	0.0%
P_2O_5	0.0%
Lo_I	0.2%

[a] Modal mineralogy and major element data from Ngwenya et al. (1990). Sample location: Locharbriggs North Quarry, Baird and Stevenson, Dumfries, Scotland.

periments. Such samples have a limited volume where deformation structures can develop free from edge effects. In this study, larger samples, 100 mm diameter, have a larger volume where structures can evolve free from edge effects, and hence can be used to investigate the spatial complexity of deformation structures on a larger scale.

We investigate the development of faulting in initially intact, cylindrical samples (100 mm diameter) of porous rock as a function of increasing axial strain at constant confining pressure (simulating a few kilometres depth). The influence of confining pressure on laboratory formed deformation band structures is treated separately in Mair (1997). Stress and strain were monitored continuously during loading and the samples, which had undergone progressive deformation, were subsequently unloaded and studied by thin section and laser particle size analysis. Zones of distinct deformation bands developed in deformed samples, with an increasing number of bands developing with increasing strain.

2. Experimental methodology

The sample rock-type used in tests was Locharbriggs sandstone, a lower Permian aeolian sandstone which is highly porous and quartz rich. A petrophysical characterisation is presented in Table 1. This sandstone is analogous to the Penrith sandstone studied by Fowles and Burley (1994). No clay is present but hematite cement exists as a coating on grains and some feldspar is present. Fresh (non-weathered) blocks were obtained from a working quarry in Dumfries, South West Scotland. Cylinders of 100 mm diameter were cored from the blocks of Locharbriggs in directions perpendicular and parallel to the lamination using a diamond coring drill. The sample ends were then lathed to produce precise right-angled cylinders of the appropriate length. All sample preparation was carried out at room temperature.

Each sample was jacketed in a rubber sleeve to isolate it from the confining fluid. The sample stack consisted of two steel mushroom-shaped platens, exactly the same size as the sample, in contact with the upper and lower ends of the sample (Fig. 1). The lower platen contacted the sample via a spacer and a thin Melinex disc coated with a lubricant as shown in the enlarged diagram (Melinex is a very strong polyester with low friction properties). This arrangement was designed to reduce end-piece friction, which may inhibit shear localisation by preventing sideways movement of the sample (Scott et al., 1994). The rubber sleeve was bonded to the platens in order to prevent leakage of confining fluid into the sample during the initial stages of loading. We assumed that negligible load can be supported by the rubber sleeve due to its weakness compared to the rock (Weeks, 1980).

The large capacity stiff triaxial deformation rig, shown schematically in Fig. 1, is used to apply axial

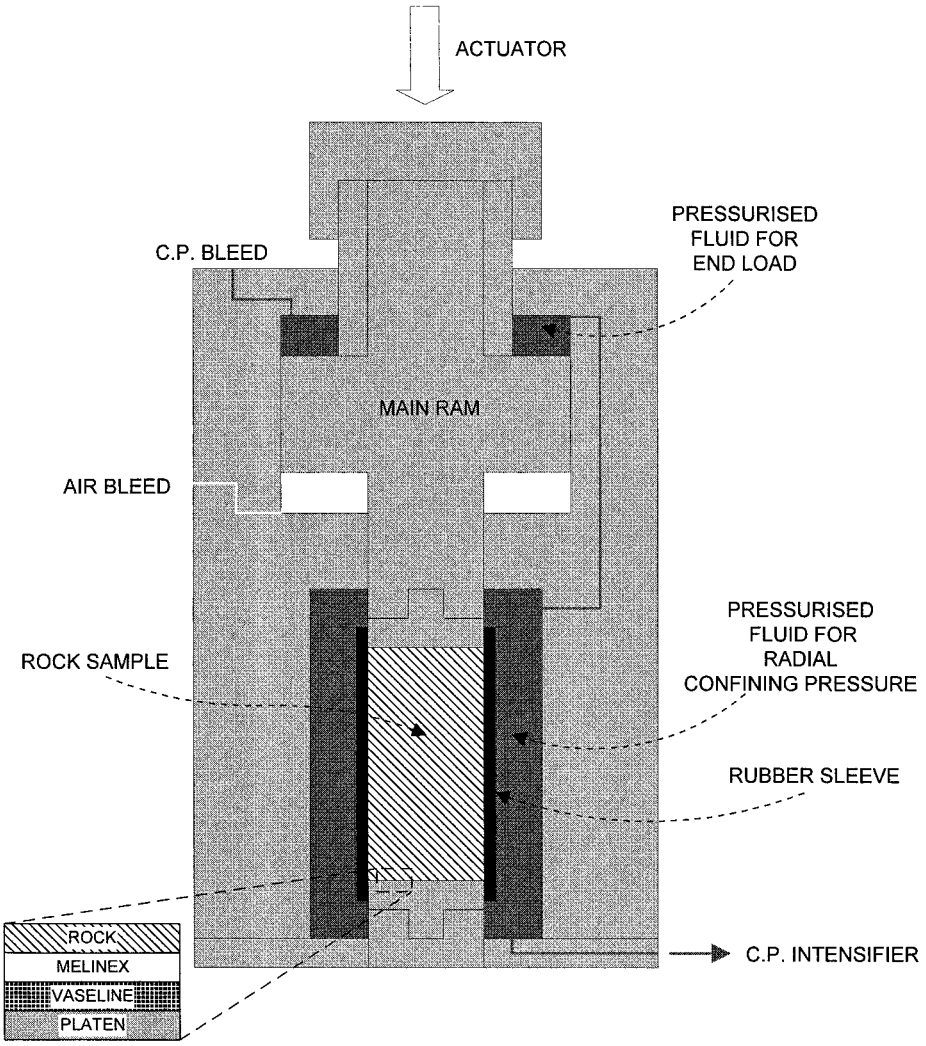

Fig. 1. Schematic diagram of the large capacity triaxial deformation apparatus. The 100-mm-diameter cylindrical rock sample located in the centre of a pressure vessel is isolated from the pressurised confining fluid by rubber jacketing. The pressurised fluid is directed to the volume behind the main ram to apply an end load equal to the confining pressure hence hydrostatic loading. Additional axial load is provided by a servo-controlled actuator. The enlarged box highlights the lubrication between the sample and the lower platen to facilitate lateral movement during deformation.

load and radial confining pressure to cylindrical samples [diameter (d) = 100 mm; length (l) = 230 mm]. The significant difference between this apparatus and others is the capacity to deform much larger dimension samples. Maximum compressive stress (σ_1) is applied axially to the parallel ends of the sample by an external servo-controlled hydraulic actuator. Minimum (σ_3) and intermediate (σ_2) stresses are equal and are achieved by pressurising the confining fluid which surrounds the sample (housed inside a pressure vessel) using a servo-controlled hydraulic intensifier rated to 10 000 psi (69 MPa). The deformation apparatus has a pressure balanced ram which means that radial confining pressure is also applied axially. This results in hydrostatic loading which prevents the sample 'necking' before axial load is applied and also reduces the magnitude of the axial load contribution required from the actuator. Loading is controlled by comparing feedback signals of ram position and pressure with command signals. If there is an error between the feedback and command signals, the ram is moved in order to reduce the discrepancy to zero. This closed loop control system enables fast and accurate loading.

The motion of the actuator is constantly monitored by displacement transducers. Axial strain throughout the test is calculated by dividing the change in the actuator position, by the initial sample length. The deformation of the testing rig itself is not taken into

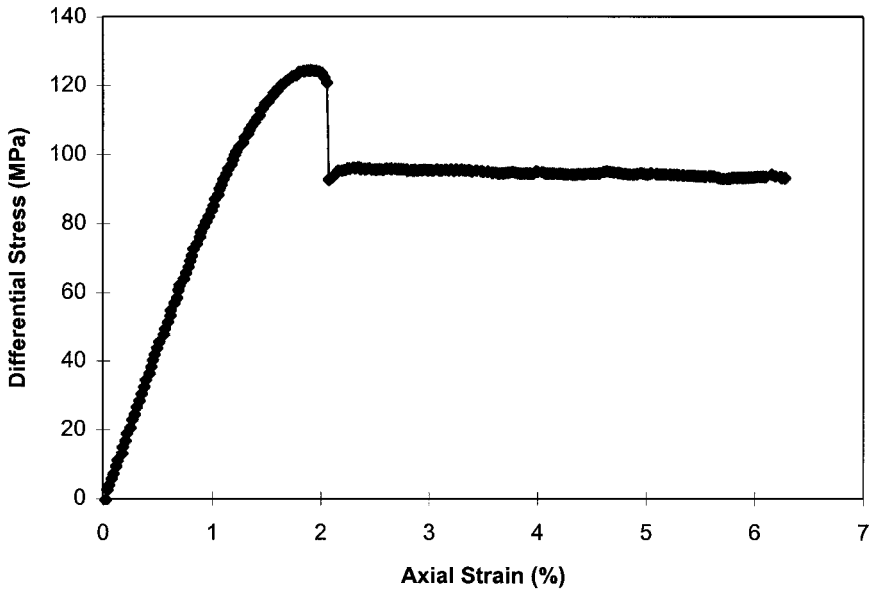

Fig. 2. Graph of differential stress (MPa) vs applied axial strain (%) for an intact dry sample of Locharbriggs sandstone deformed at 5×10^{-6} s^{-1} axial strain rate. The curve shows typical characteristics of all the samples tested.

account during this calculation. The apparatus has a stiffness of 1.05×10^9 N/m which is used to calculate the effects of rig deformation on axial strain in the Appendix. Internal and external load cells are used to measure the total axial force applied to the ends of the sample. Axial stress is calculated by dividing the load measured at the internal load cell, by the initial cross-sectional area of the sample. It is assumed that the sample cross-sectional area of the sample remains constant until the sample fails (Scott et al., 1994) which is a reasonable approximation within an error of a few percent in stress. Volumetric strain can be monitored throughout a test by measuring the differences in the volume of confining pressure fluid required to maintain constant confining pressure. Volumetric strain data are not presented in this paper but are treated in Mair (1997).

The testing procedure involved the application of confining pressure (hence hydrostatic load) of 34 MPa (5000 psi) followed by a period of equilibration before the application of differential load. The tests were all carried out at a constant axial strain rate of 5×10^{-6} s^{-1} and at room temperature and humidity with no pore fluid present. The main ram was controlled under displacement (stroke) control and was advanced at a constant velocity until a pre-determined position was reached. All the tests presented (with the exception of one test which was terminated immediately prior to failure) underwent dynamic failure then increasing amounts of post-failure deformation. In this way we investigated the effects of post-failure strain on deformation structures. After each experiment, load was removed then the sample was carefully unloaded for structural analysis.

3. Results

3.1. Mechanical data

Fig. 2 shows a typical stress–strain curve plotted as applied axial strain (%) vs differential stress (σ_1–σ_3) (MPa) which highlights the key features exhibited by

Table 2
Experiments[a]

Expt	ε_{total} (%)	Length (mm)	Peak σ_1–σ_3 (MPa)	$\varepsilon_{at\ failure}$ (%)
Bedding parallel to sample axis				
R5	4.22	189.5	120.6	1.77
R1	6.34	205	124.4	2.03
R6*	6.50	192.5	116.9	1.62
R3	9.16	192	118.2	1.92
Bedding perpendicular to sample axis				
R13	1.5	229	133.9	n/a
R14	1.75	227	130.9	1.50
R12	2.0	229	134.7	1.58
R15	3.0	229	137.2	1.66
R16	8.0	228.5	136.6	1.50
R2	11.2	205	139.8	1.73

[a] Tests all have sample diameter = 100 mm, confining pressure = 34.5 MPa, pore pressure = 0 MPa, axial strain rate = 5×10^{-6} s^{-1} except where stated. (*Axial strain rate = 2.5×10^{-6} s^{-1}.) ε is axial strain uncorrected for rig stiffness (see Appendix for stiffness correction).

all the tests considered here. After a short period of crack or pore closure indicated by the concave up curve on initial loading, linear elastic behaviour extends for the majority of the pre-failure stage. At approximately two thirds of the peak stress, the graph departs from linearity, demonstrating strain hardening behaviour most likely due to microscopic inelastic processes. Peak (or ultimate) stress is followed by a short period of strain softening (where the graph curves downward). A measurable (and often audible) stress drop marks sample failure which we refer to as dynamic due to its rapid nature. Following dynamic failure, which occurs at approximately 1.75% axial strain, behaviour is characterised by small fluctuations about a fairly constant value of axial stress which is consistent with quasi-static frictional sliding. No obvious phase of strain hardening or softening is observed during the post-failure stage. All tests conducted show the similar characteristics irrespective of bedding orientation, however, tests with samples having bedding perpendicular to length are approximately 20 MPa stronger than those with bedding parallel. Table 2 summarises the experimental data for each test. These mechanical observations agree with many previous experimental studies of brittle failure in rocks, e.g. Paterson (1978), Bernabe and Brace (1990), Wong et al. (1997).

3.2. Structural analysis techniques

Samples deformed to increasing amounts of axial strain (see Table 2) were carefully removed from the loading apparatus for microstructural analysis. Initially, samples were kept in their rubber jackets to avoid damage. The major characteristics of the deformation, generally a visible offset between the hanging wall and footwall implying shear failure, were observable through the opaque jackets. All the samples showed evidence of macroscopic shear failure (along one plane as opposed to a conjugate set) with the exception of R13 which was terminated prior to failure (see Table 2). In order to expose the fault zone, the jacketed samples were cut in half radially (at the midpoint of the fault zone) using a hand saw. The cutting procedure was carried out dry, at room temperature and ambient humidity, to prevent fine gouge material being washed away. The exposed radial sections were photographed and measured before one half of each sample was impregnated with low viscosity epoxy resin for thin sectioning and the other half was disaggregated for laser particle size analysis. Through a combined approach of two-dimensional and three-dimensional analyses we aim to exploit the strengths of both techniques to reveal more about the deformation processes.

Large-scale thin sections (75 × 50 mm) were cut parallel to σ_1 and in a plane perpendicular to the fault zone. This orientation permitted analysis of damage inside the fault zone along dip and with distance away from the fault zone in the surrounding rock. Some thin sections were impregnated with blue epoxy resin to aid the identification and quantification of pore space. Initial analysis of the thin sections was carried out using a low magnification macroscope which

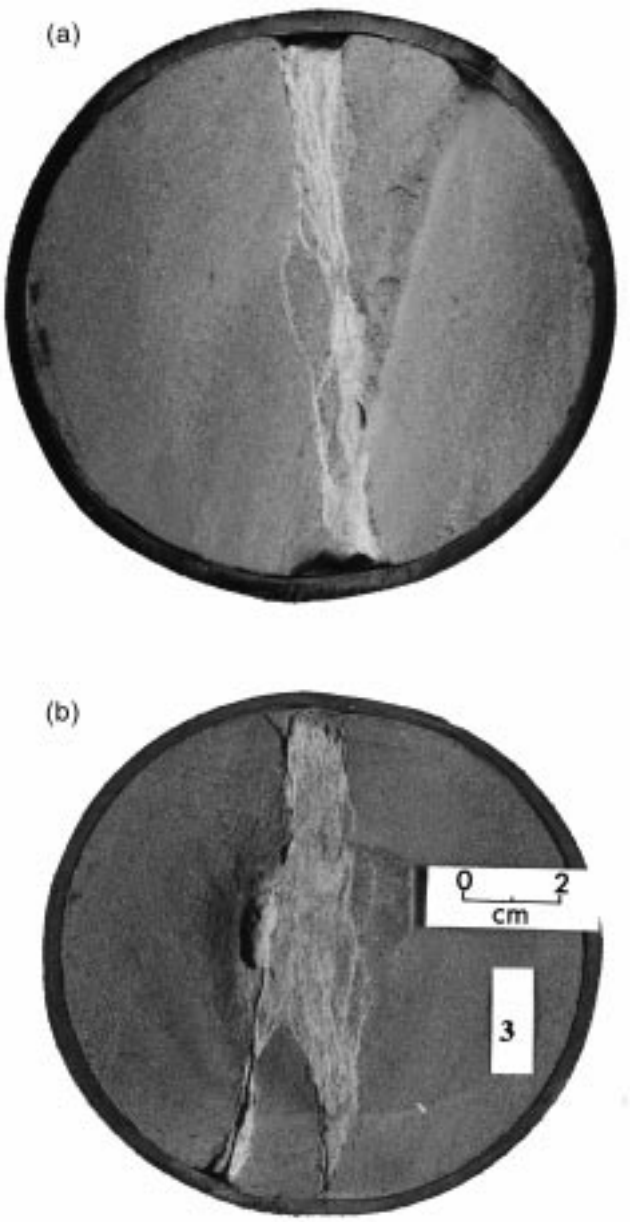

Fig. 3. Photographs showing radial cross-sections of Locharbriggs sandstone samples deformed to (a) 6.0% and (b) 9.0% final axial strain. Samples are 100 mm in diameter, σ_1 is perpendicular to the plane of the photograph, and confining pressure (σ_3) is applied round the circumference of the sample, in a plane parallel to the photograph. Note the deformation is expressed as a series of pale interweaving strands in both cases but in (b) the fault zone is wider and consists of a larger number of discrete strands.

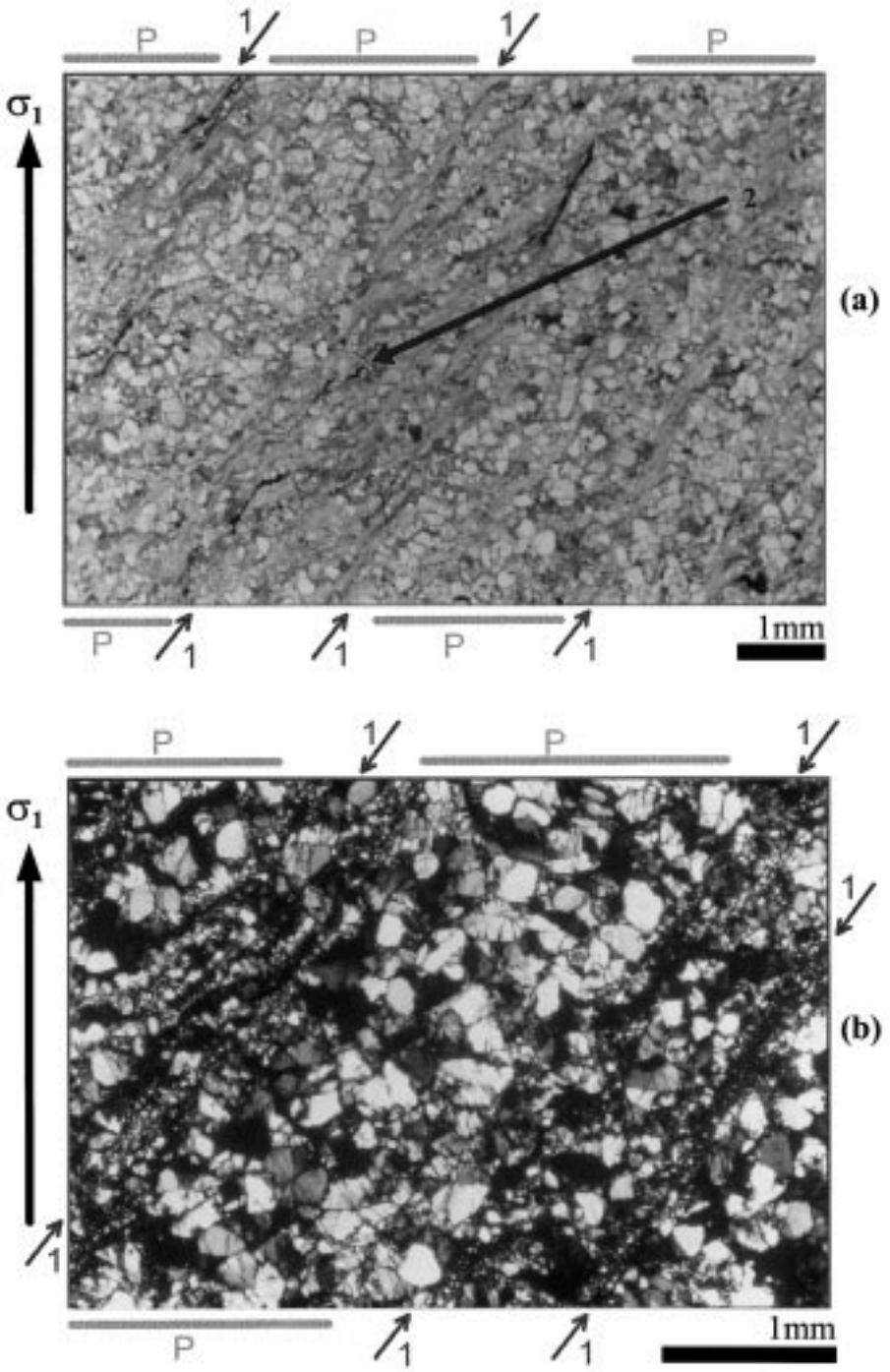

Fig. 4. Photomicrographs of a thin section cut parallel to σ_1. The sample was shortened by 11.22% axial strain. σ_1 is vertical and $\sigma_2 = \sigma_3$ is in the horizontal plane. (a) Under plane polarised light, several fine grained gouge strands (arrow 1) with internal structure (arrow 2) are separated by pods of host rock (P). (b) Under crossed polarisers at higher magnification, the grain-size reduction in the gouge strands (arrow 1) compared to the pods (P) is clear. Note also the pervasive microcracking in the fault zone pods (P).

allowed a wide field of view and was therefore extremely useful in identifying microstructural fabrics and spatial relations. A standard petrological microscope was subsequently used for more detailed analysis on the grainscale.

We studied the grain-size distribution of the individual fault strands relative to the host rock using a Coulter LS100 Laser Particle Size Analyser. This apparatus exploits the principle that the angle of diffraction of laser light is influenced by the size of particles in its path. A disaggregated sample suspended in a solution of distilled water is passed between a laser source

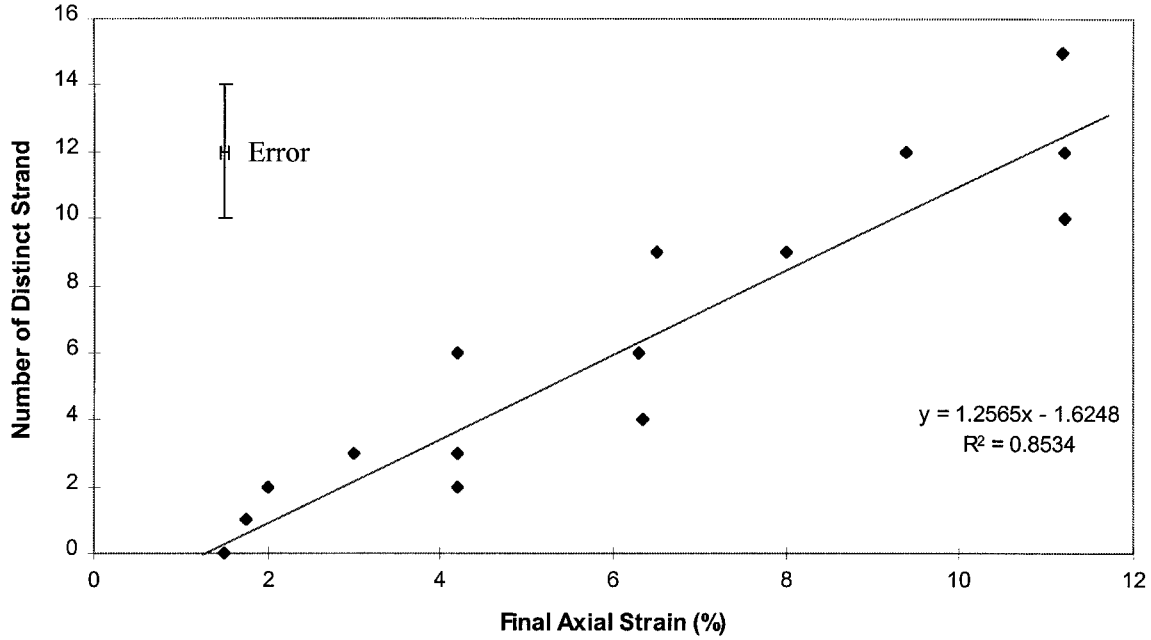

Fig. 5. Graph showing the number of distinct gouge strands vs final applied axial strain (%) measured from exposed radial hand specimen sections (Fig. 3) and horizontal point count transects across thin sections (Fig. 4) using ×10 magnification. An estimated error bound for the primary data is shown on the graph, together with the best-fit straight line. The data show a good linear correlation of increasing numbers of strands for increasing applied axial strain (solid line).

and a detector. The collimated laser beam is diffracted by each particle, by an amount related to the curvature and the refractive index (R.I.) of that particular grain. Assuming the grains are all spherical and have the same R.I., the angle of diffraction will be a function of the grain radius. Small particles cause higher angle diffractions than larger particles and hence the diffraction data may be used to calculate grain size distributions. The composite flux pattern produced due to many diffractions from different sized particles is decomposed using a Fourier lens and the number particles of a given radius is measured. Advantages of this technique include: the broad range of grain sizes (from 0.4 to 800 μm diameter) that can be measured simultaneously; the higher resolution compared to an optical microscope; the speed of measurement (compared to sieving and settling techniques); and the fact that the measurement is three-dimensional. Disadvantages are the assumption that all grains are spherical and have an equal R.I.; and the loss of a spatial relationship between grains. These assumptions may be problematic for highly angular fractured grains resulting in an overestimate of their size.

3.3. Structural observations

Fig. 3(a) is a photograph showing the radial cross-section (perpendicular to σ_1 and parallel to $\sigma_2 = \sigma_3$) of a sample deformed by 6% axial strain. Deformation is expressed as a series of distinct fault strands which form one macroscopic zone of damage ~10 mm wide. The individual fault strands are pale, <1 mm wide and interweave with each other. Between these strands are lenses of apparently undamaged host rock caught up inside the fault zone. Fig. 3(b) shows a similar radial cross-section for a sample deformed further to 9% axial strain. The deformation has comparable characteristics, however, in this sample the fault zone is wider (~20 mm, compared to 10 mm) and is composed of a greater number of discrete strands (12 strands as opposed to six strands).

Fig. 4 shows photomicrographs of part of a laboratory induced fault zone. The direction of σ_1 is vertical as shown and $\sigma_3 = \sigma_2$ is in the horizontal plane. This particular sample was shortened by 11% axial strain at the conditions described for R2 in Table 2. Distinct pale strands are clear (see arrow 1) and occur sub-parallel to each other at angles of less than 045° to σ_1. There is a significant reduction in grain size inside these strands which will therefore be termed 'gouge strands'. Within the individual strands, structures can be identified. The structure manifests itself as zones of ultrafine gouge parallel to the strands or linear 'stringers' of brown, very fine grained material (opaque under cross polarisers) lying oblique to the strands (see arrow 2). Longitudinally continuous lenses of host rock, referred to as 'pods', are situated between the gouge strands and show significant grain fracture. The gouge strands are commonly 300 μm in width compared to the pods of host rock which are approxi-

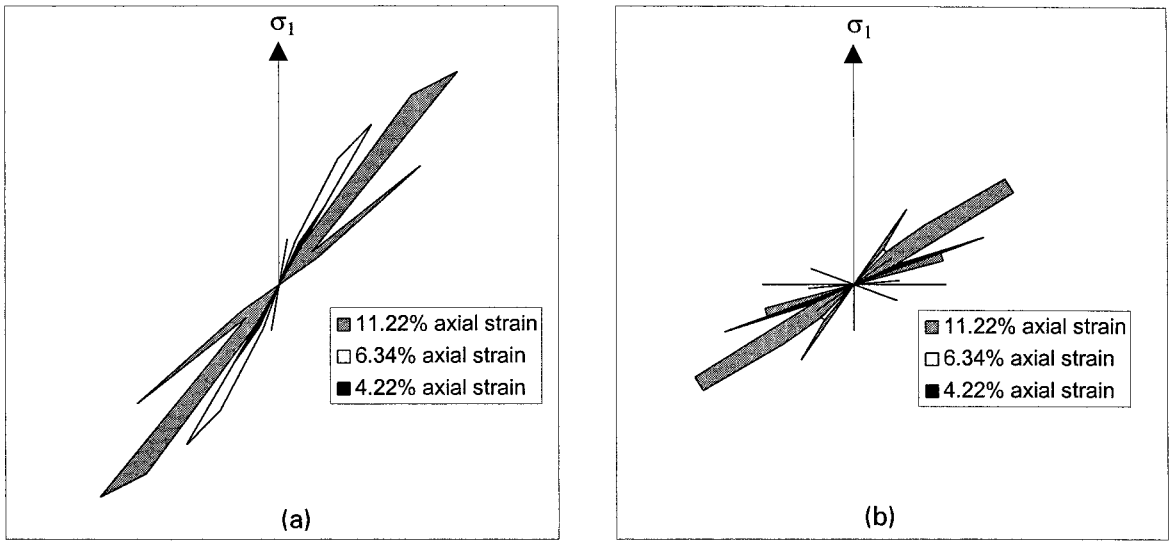

Fig. 6. Rose diagram plots showing the frequency distribution of the orientation of (a) gouge strands (Fig. 4a, arrow 1), and (b) structure within the strands (Fig. 4a, arrow 2) with respect to σ_1. The angle is plotted clockwise from σ_1 at 000°, in 5° bins, and the length of the 'petals' are proportional to the frequency. The mean orientation of the strands is approximately 030°, and the internal structure within the strands trends at approximately 060°. Data from three samples deformed by different axial strains all show comparable trends, indicating no evidence for rotation associated with increased strain.

mately 800 μm wide. Although the respective widths do vary, the fault zone pods are always wider than the individual gouge strands.

We quantified progressive deformation as a function of axial strain by counting the number of discrete strands forming the fault zone in each sample. Radial cross-sections and longitudinal thin sections were analysed using ×10 magnification to distinguish individual

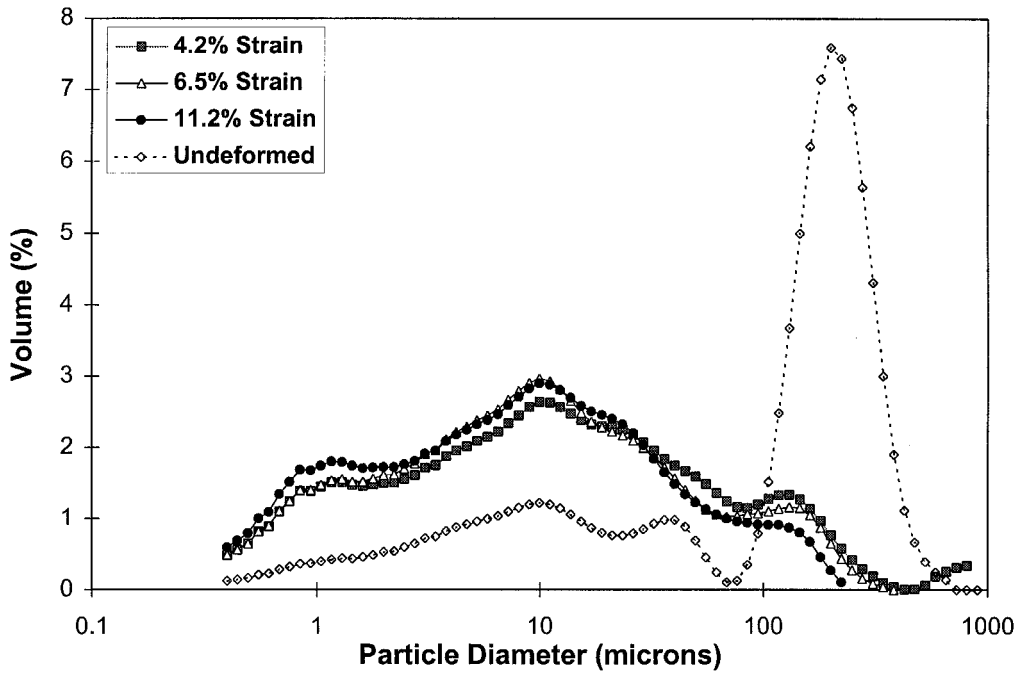

Fig. 7. Graph of incremental total volume (%) vs grain diameter (μm) from the laser particle size analysis on a log linear scale. The plot compares the grain-size distributions of gouge strands sampled from tests carried out at increasing amounts of axial strain (4.2, 6.5 and 11.2%). The grain-size distribution for undeformed Locharbriggs sandstone is plotted for comparison. The three gouge samples have very similar characteristic curves which exhibit both the same peak value, indicating significant grain-size reduction with respect to the undeformed sample, and a similar range of grain sizes.

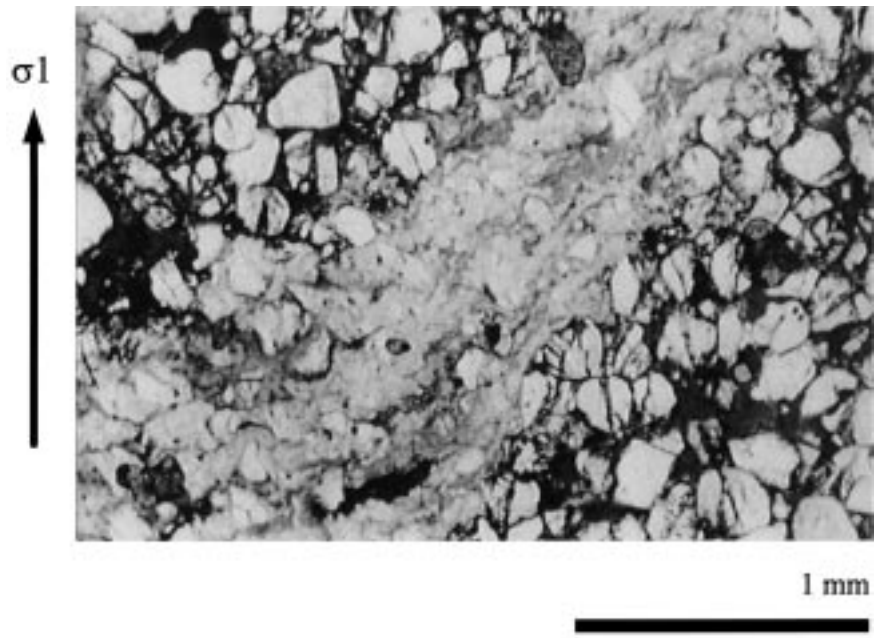

Fig. 8. Photomicrograph showing thin section which has been impregnated with coloured epoxy resin in order to highlight the pore space. The frame shows part of a fault zone containing one gouge strand (trending top right to bottom left) and two adjacent fault zone pods. σ_1 is vertical and the sample was deformed by 11.2% strain. The fault zone pods show good epoxy impregnation gouge (black areas), whereas the gouge strand is conspicuous due to its total lack of epoxy impregnation.

strands. Every gouge strand encountered on a perpendicular transect across the middle of the fault zone was counted. Fig. 5 shows the number of distinct gouge strands as a function of final applied axial strain (%). Note that R13 terminated prior to dynamic sample failure at 1.5% strain shows no gouge strands. An estimated error bound and best-fit linear regression are displayed on the graph. The data show a very good positive correlation between increasing numbers of strands and increasing applied axial strain.

Fig. 6(a) is a rose diagram showing the orientation of gouge strands with respect to σ_1. Orientation is measured by transects carried out on thin sections from samples subjected to increasing axial strains. The rose diagram is basically a circular histogram with orientation plotted clockwise with respect to σ_1 at 000°. Data are organised into 5° intervals (bins) and the length of petals is proportional to the frequency in each bin. The gouge strands show a dominant trend at 030° to σ_1. The data show little scatter indicating the strands are sub-parallel and there is no obvious rotation of deformation with increasing axial strain. Fig. 6(b) shows the orientation of a secondary structure within the gouge strands. This structure trends at 060° with respect to σ_1 and at 30° to the gouge strands themselves.

Fig. 7 shows a comparison of the grain-size distribution by volume in gouge strands from R5, R6 and R2 subjected to 4.2, 6.5 and 11.2% axial strain, respectively. Each gouge strand selected for study was randomly chosen from a separate deformed sample. The grain-size distribution data for undeformed Locharbriggs host rock are plotted for comparison. The data for the undeformed host rock and the gouge strand specimens are both characterised by approximate bell-shaped curves with main peaks at 200 and 9.97 μm, respectively, interpreted as the most frequent grain diameters. The data indicate a dramatic reduction in peak grain diameter in the gouge strands with respect to the host rock. Also, the gouge strand curves have a much wider range of grain sizes than the host rock, indicating reduced sorting. The fine details of the gouge strand curves may differ for different strains (see Fig. 7) but the main characteristics are strikingly similar. The peak grain size of 9.97 μm measured in one gouge strand is similar to that for a gouge strand from a different sample irrespective of the total axial strain applied to the bulk samples. The widths of the peaks in all three samples are also similar suggesting a similar degree of sorting.

3.4. Point count analysis

In order to obtain an unbiased quantitative analysis of the fault zone and host rock, we used a point counting technique on thin sections. A series of linear point count transects were carried out in orientations parallel or perpendicular to the σ_1 and also parallel to the trend of the fault zone, with the grains analysed (counts) per transect varying from 30 to 150. Here a

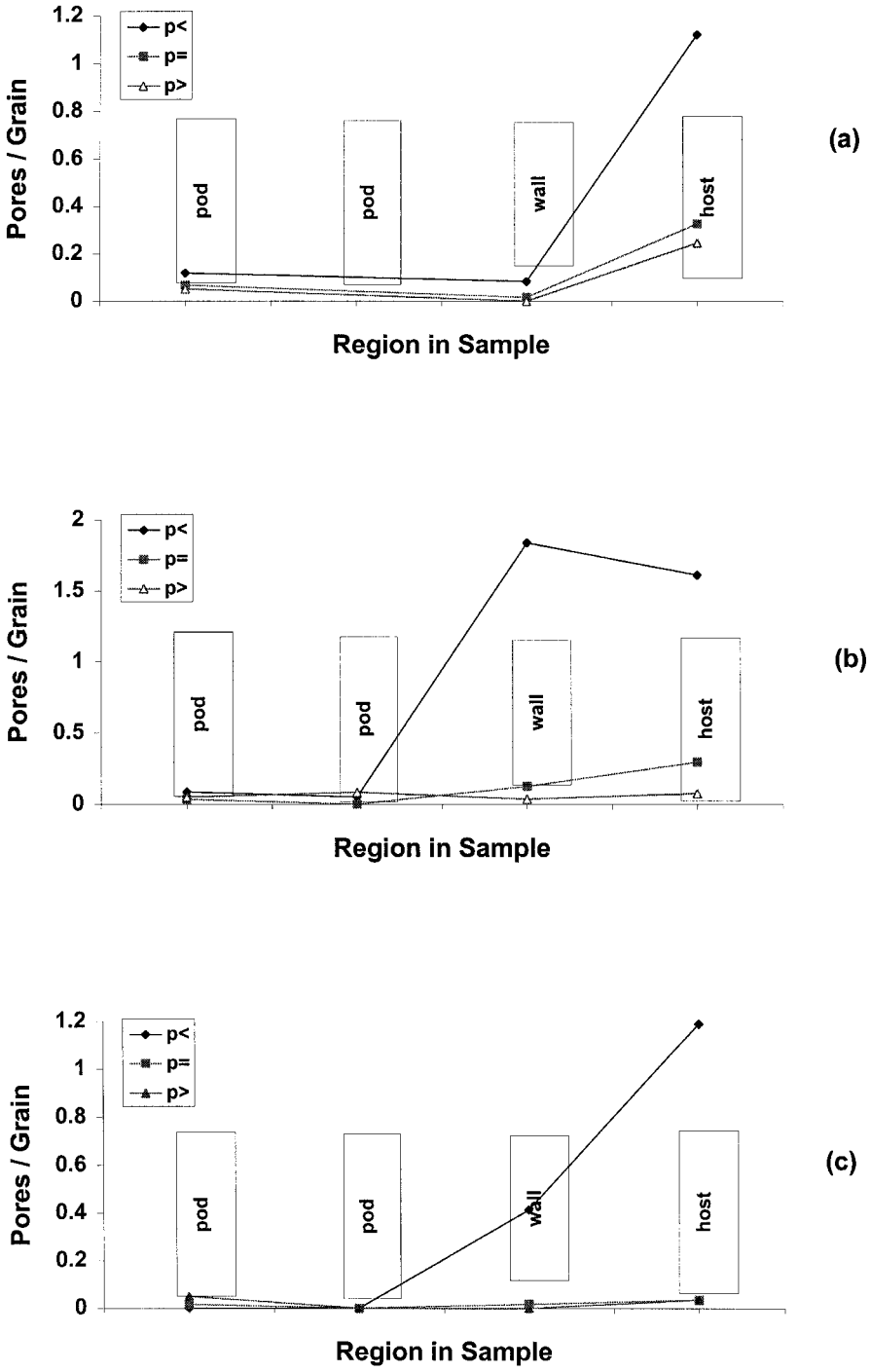

Fig. 9. (a)–(c) Graphs of point count data showing the neighbouring pore space per grain vs the position or region of the sample, i.e. host rock, wall rock, fault zone pod. Data are presented for samples deformed to: (a) 4.2%; (b) 6.5%; and (c) 11.2% axial strain. Data are spilt up into three subsets of pores which are larger (>), equal to (=) and smaller (<) in size than the cross hair grain. Note that most pores are smaller than the grains and there is a definite reduction in pore space in the fault zone with respect to the host rock.

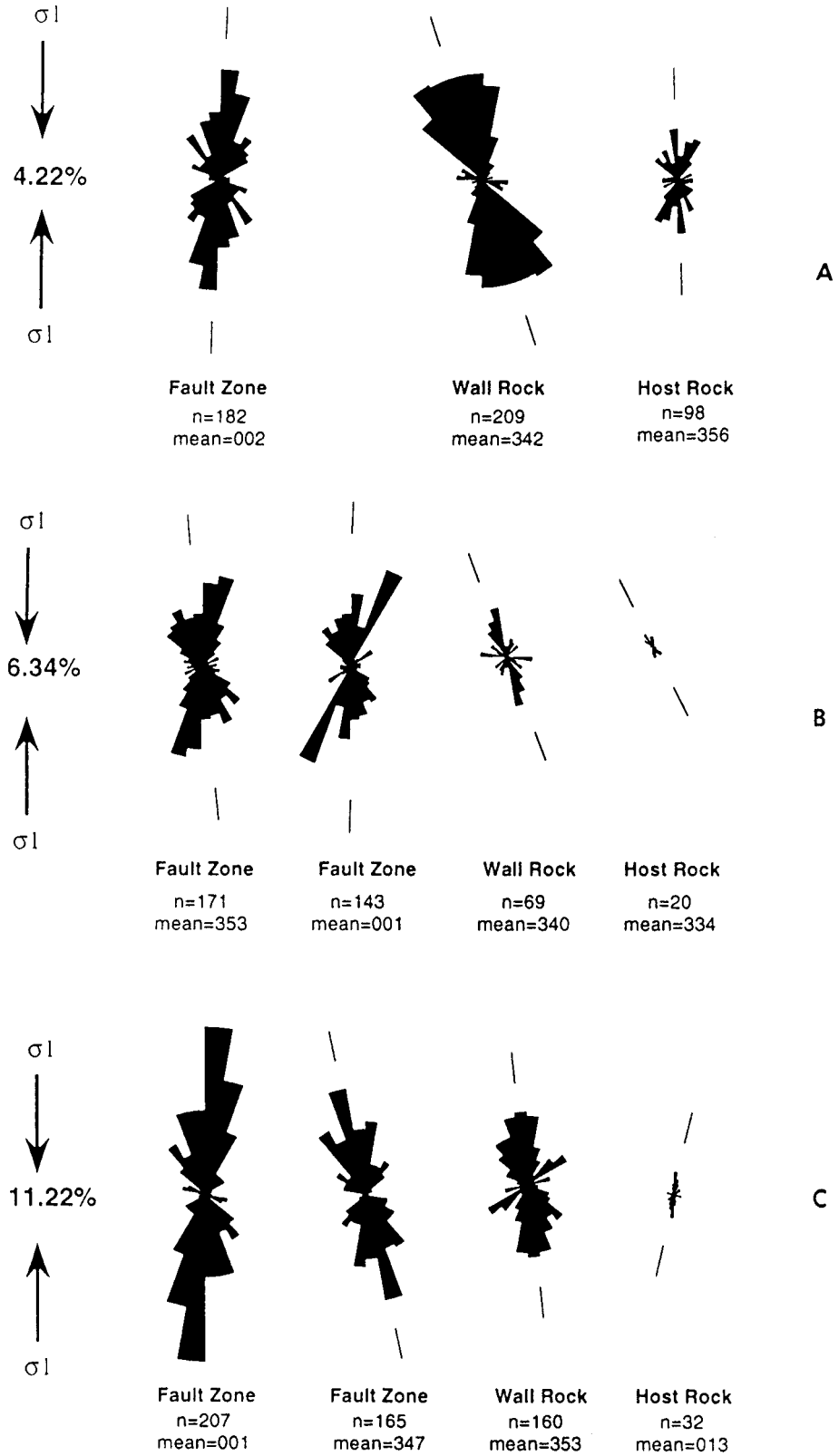

Fig. 10. (a)–(c) Rose diagrams show the orientation and abundance of microcracks in the fault zone pods, wall rock and host rock of three samples. (a) Data for sample R5; (b) data from R1; and (c) data for R2. These rose diagrams have the equivalent bin sizes of 10° and frequency is proportional to the length of the petals. n is the number of microcracks. The mean orientation is also presented.

standard petrological microscope, with magnification of ×4, ×10, ×40, was used to analyse individual grains. In these transects, we recorded the grain diameter, shape and fracturing as well as information on the pores and grains surrounding each 'cross hair' grain. Properties such as the grain size, pore size, width of gouge strands were measured using an optical micrometer.

We showed in Fig. 7 that the grain size in gouge strands is significantly reduced with respect to the host rock. A reduction in grain size alone will not necessarily cause a reduction in porosity if the grain shape, sorting and packing remain constant. However, sorting is clearly different in the gouge strands and host rock (Fig. 7) and this will certainly affect the porosity in the strand. To highlight and quantify the pore space, thin section samples were impregnated with coloured epoxy resin. Fig. 8 is a photomicrograph, with σ_1 vertical, showing part of a larger fault zone containing both fault zone pods and gouge strands. Epoxy resin (black areas) is clearly observed in the fault zone pods and also in the host rock 10 mm away from the fault zone (not shown) suggesting significant porosity in both regions. In contrast, no epoxy resin has impregnated the gouge strands. This implies that the porosity and hence permeability of the gouge strands is much smaller than both the fault zone pods and the host rock. The absence of resin impregnation precludes measurement of pore space within the gouge strands by point counting but it does imply that porosity is extremely small here compared to the host rock.

The skeleton (or primary) porosity in the pods and the host rock was measured in a series of transects by point counting the pore space neighbouring each cross hair grain. The voids filled with coloured epoxy are generally sub-rounded since the secondary porosity due to microcracks was not included (this is considered separately later). The pore space was divided into sizes smaller than, equal to and larger in diameter than the grain under the cross hairs. The graphs in Fig. 9(a)–(c) show the mean number of neighbouring pores per grain in different areas of the sample for pore sizes greater than, equal to and smaller than the cross hair grain. The transects here were all measured in directions parallel to the trend of the fault zones and were taken in: (i) the host rock, 10–12 mm away from the fault zone edge; (ii) the wall rock defined as the region adjacent to the fault zone, 5–10 grain diameters wide where the density of microcracks is notably higher than in the host; (iii) a pod near the edge of the fault zone; and (iv) a pod in the middle of the fault zone. The x-axes indicate the type location of transects. Although these data cannot be directly converted into a porosity (without a series of assumptions concerning grain shape and packing), they do give a quantitative indication of the amount and nature of pore space surrounding the grains in different parts of the sample.

The consistent finding from the analysis presented here confirms that the amount of pore space in pods located at the centre and edge of the fault zone is seriously diminished compared to the pore space measured in the host rock. In general, the majority of the pore space in the wall rock is smaller than the size of the grain. In two cases the pore space in the wall rock adjacent to the fault zone is reduced but in the third it is actually enhanced relative to the host rock. This increase may imply some dilatant effect. There is no direct correlation between the porosity in fault zone pods and the applied axial strain. In summary, the permeability in the gouge strands is qualitatively much lower than in the adjacent fault zone pods (Fig. 8). Similarly the pods show a lower amount of pore space than the host rock, hence gouge strands are interpreted to have significantly reduced porosity and permeability with respect to the host rock.

On initial inspection of hand specimens it appeared that the fault zone pods occurring between the gouge strands were lenses of undamaged host rock caught up in the fault zone. Under microscopic investigation however, these pods show significant microcracking within grains. This is highlighted in the photomicrograph in Fig. 4(b). The microfractures commonly extend across the diameter of one or more grains. Most grains are still intact but show significant damage through multiple fractures.

To measure the density and orientation of microcracks in the fault zone pods, linear point counting transects were carried out parallel to the fault zone trend. The density of cracking was also measured as a function of distance away from the fault, in the wall rock and the host rock. During this analysis, microcrack damage within grains was differentiated into minor fractures and major through-going fractures. Both minor and major microfractures are superimposed here as they have comparable trends. Rose diagrams (Fig. 10a–c) show the orientation of microfractures with respect to σ_1 in different parts of the fault zone. The largest proportion of microcracks per grain are found in the fault zone pods. There is a definite microcrack anisotropy as cracks are predominantly oriented sub-parallel to σ_1. In the wall rock there is still an enhanced microfracture density which is approximately axial in orientation. Outside this wall rock zone the density of cracks diminishes markedly to the background level. Microcracks in the wall rock are pervasive, up to approximately 5–10 grain diameters out into the host rock irrespective of the axial strain applied to the host rock. In contrast to the intensive microcracking in the pods, there is a distinct lack of microfractures in the original grains caught up in the gouge strands.

4. Discussion

4.1. Comparison to previous field and laboratory observations

In this section we discuss our laboratory results with reference to previous observations and theories. We have produced individual gouge strands which anastamose in plan view (perpendicular to the fault plane) and lie parallel to each other in the plane of the slip direction. The deformation band structures presented in this paper are produced in a highly porous, quartz-rich, clay free sandstone at a confining pressure of 34 MPa. Interestingly, this pressure lies in the range (20–50 MPa) estimated for the stress field in the Entrada Formation in Arches National Park, at the time of deformation band formation (Antonellini et al., 1994). Hence our experimental conditions may be a good analogue for natural conditions where certain types of deformation bands form in highly porous, quartz-rich sands.

Our laboratory tests show decisively a discrete, hierarchical development of more strands and a wider fault zone for increased amounts of axial strain. This agrees with observations of the offset on bedding across zones of deformation bands in the field (Aydin and Johnson, 1983), and is the first time that such a positive comparison has been made with laboratory tests. Significantly, there is a linear relationship between number of strands and applied axial strain, and an absence of strands at the axial strain corresponding to dynamic failure (Fig. 5). This relationship implies that there were no strands before the point of failure, and that the number of strands then increased linearly as a function of strain during the post-failure period. The implied absence of strands prior to failure was tested by examining a sample from a test halted just prior to failure: no strands had formed. This internal consistency is reassuring.

Individual gouge strands show grain-size reduction and an increase in grain angularity with respect to the host rock implying that brittle cataclastic mechanisms (grain crushing and grinding) are active in the fault zone. The occurrence of microcracks in the fault zone pods and in the wall rock is further evidence of brittle micromechanisms. Macroscopic brittle behaviour is also exhibited by the stress–strain curves and the observation of fairly localised faulting. Structures, within the gouge strands (Fig. 4a, arrow 2), referred to as stringers are further evidence for movement along these gouge strands. The orientation of these structures with respect to σ_1 means it is not appropriate to interpret them as Riedel shears unless significant local stress rotation has occurred. These stringers are similar to generic shear zone features described (Antonellini et al., 1994) as bedding planes which have been smeared out along shear zones. The bedding planes in our samples can be identified through their concentrations of hematite. The stringers we observe in the laboratory would be consistent with hematite smeared out in a similar way and would indicate more displacement occurring near the edges of the gouge strands. This yields a sense of slip which is consistent with the macroscopic shortening direction and also suggests differential amounts of slip inside a single band.

The mean grain size within the gouge strands is reduced to the same degree in a random strand regardless of the total bulk strain applied to a sample. If granulation is proportional to the amount of displacement along a strand, this suggests that each strand is accommodating a similar and finite slip with further deformation requiring new strands. From our correlation between number of strands and axial strain this is reasonable and could be interpreted by a strain hardening mechanism. Engelder (1974) suggested that granulation is initially intense, and closely associated with slip, but subsequently levels off asymptotically with further slips, having little effect on comminution. The latter case invokes a grinding limit (steady state) where a favourable grain size distribution is reached and where further displacement is accommodated without significant grain fracture. In this scenario displacement cannot necessarily be interpreted from mean grain size. Although material is still evolving, mean grain size is changing very slowly.

Sorting within the individual strands is reduced with respect to the host rock (Fig. 7), the gouge material having a much wider spread of grain sizes. When plotted as size distribution by number on a log graph, the gouge material is best fit by two separate power-law curves for the size ranges $<10\ \mu m$ and $>10\ \mu m$, respectively (Mair, 1997). The exponents of these curves are equivalent to apparent fractal dimensions and hence indicate a binomial fractal size distribution. This is consistent with the observations of Biegel et al. (1989) and Marone and Scholz (1989) which showed that the grain-size distribution of fault gouge can evolve through granulation to a fractal size distribution. The original grains caught up in the gouge strands of our test samples show very little fracturing in comparison to the adjacent fault zone pods which are pervasively fractured. Importantly, gouge strands have a *matrix-supported* fabric, where large grains are surrounded by a sea of smaller particles. This observation agrees with theories of Sammis et al. (1987) and Biegel et al. (1989) that the probability of fracture decreases as the size of neighbours decreases, hence large grains cushioned by smaller ones are less likely to fracture. Marone and Scholz (1989) also observed, in the laboratory, that grains reduced to a certain size actually appear stronger. Grains located in the fault zone pods of our samples are of uniform size, have

very little surrounding matrix (hence are *grain-supported*) and show extensive microcracking. These regions clearly demonstrate the idea that grains of equivalent size lying adjacent will tend to result in one of the grains fracturing (Biegel et al., 1989).

The evolution in grain-size distribution may have important implications for the shear resistance of the gouge strands. The exact nature of this relationship is subtle, complex and poorly understood to date, however, laboratory studies of sliding on a well-defined gouge zone (Biegel et al., 1989) provide evidence that under certain conditions, finer gouge has a higher value of friction and greater compaction than coarse gouge. Gu and Wong (1994) also correlate an increase in friction with enhanced compaction in gouge layers. It is intuitive that a fractal gouge will pack and hence compact more efficiently than grains of equal size. This will increase the number of grain contacts hence increasing contact friction within the bands providing a potential hardening mechanism for individual strands which appears consistent with our experiments.

The orientation of microcracks observed in our tests (sub-parallel to σ_1) is consistent, according to Coulomb failure, with extensional fractures formed during the inelastic loading phase (Fig. 2) and, e.g. Paterson (1978). From volumetric strain data, Mair (1997) interprets dilatancy during this stage. The Coulomb failure criterion also predicts shear fractures with no tensile component orientated at 30° to σ_1 which is consistent with the orientation of the gouge strands we produced in the laboratory. Microcracks are commonly observed in the laboratory associated with macroscopic shear during brittle deformation (e.g. Dunn et al., 1973; Engelder, 1974). There is some debate over whether the axial cracks form a 'process zone' prior to shear fracture (Dunn et al., 1973), or a 'wake' of damage after shear fracture (Friedman and Logan, 1970). Studies of acoustic emission (Lockner et al., 1991) and microscopic analysis (Menendez et al., 1996) have revealed evidence for significant microcracking prior to macroscopic shear failure, consistent with the 'process zone' ideas. We have observed some evidence of shear movement along a cracked grain, implying that a tensile crack formed early during shear zone evolution was subsequently influenced by the shearing process. We attempted to investigate the rotation of cracked grains within the gouge strands for evidence of timing, however, very few larger grains in the gouge strands were fractured, most likely due to the cushioning effect of smaller particles mentioned above or possibly because the grains themselves were remnants of larger cracked grains.

Microcrack damage in the wall rock extends 5–10 grain diameters out from the edge of the fault zone for all samples studied here, irrespective of the total fault zone width. This distance is comparable to the damage observed in experimental studies of Coconino sandstone by Engelder (1974). Although we have presented evidence supporting 'process zone' ideas, it is difficult to imagine that the observed halo of microcrack damage surrounding laboratory fault zones forms prior to macroscopic failure, since it is unclear at this stage how much strain will be applied and, therefore, how wide the final fault zone will be. Instead, we believe that microcracking is ongoing as the fault zone grows in width and therefore may be intimately associated with the formation of each new shear band.

Although microcracking is often not obvious in the field near deformation bands, this may be due to subsequent healing which masks the features. Despite this, microcracking adjacent to field examples of deformation bands has been observed under the optical microscope (Antonellini et al., 1994) in sandstones from the Valley of Fire, Nevada. Also, Fowles and Burley (1994) identified microcracks and evidence for crack healing in Penrith sandstone by using a cathode luminescence technique. In summary, field investigation may tend to underestimate original microcrack densities due to overprinting. All the above evidence from our laboratory tests agrees with field observations of zones of deformation bands (e.g. Aydin and Johnson, 1978; Mair, 1997).

Significantly, we see no laboratory evidence for deformation localised onto a single slip surface at higher strains. If we consider zones of deformation bands as a form of cataclastic flow mechanism which may be a transient phenomenon replaced by shear localisation at high strains (Hirth and Tullis, 1989), our observations indicate that the transition to highly localised slip must occur at strains greater than 11.2% (at least for the experimental conditions studied here).

4.2. Model for deformation band formation

Aydin and Johnson (1983) invoked the theory of strain hardening materials, developed by Rudnicki and Rice (1975), to explain field observations of multiple deformation bands. Although this theory is consistent with our laboratory structural data, it is inconsistent with the form of the macroscopic load curves (Fig. 2). We observe strain hardening prior to failure then a stress drop at macroscopic failure before essentially constant stress, i.e. frictional sliding with additional strain (small fluctuations in the post-failure curve are interpreted as minor stress drops). There is no clear evidence for a macroscopic strain hardening episode (or episodes) after failure when we believe the gouge strands form. Therefore a simple macroscopic strain hardening model is not sufficient to describe deformation band formation in the laboratory.

One explanation is that gouge strand formation is associated with *local* strain hardening and softening

processes below the resolution of our macroscopic load curve. It is plausible that local stresses within the developing fault zone are significantly different (both larger and smaller) than the bulk properties measured at the sample ends, especially after sample failure (e.g. Jaeger and Cook, 1979; Rice, 1992). The implication is that local stress concentrations could approach sample failure stress as new strands form, without necessarily yielding a macroscopic stress signal. An alternative explanation is that several bands are active simultaneously, although their evolution is out of phase. The local strain hardening associated with a strand locking up (dying) balances the local strain softening related to the formation of a 'new' strand thereby cancelling each other out and giving no net signal on the macroscopic load curve.

The stress drop at dynamic failure is larger than the minor stress drops after failure since it is associated with macroscopic sample failure. If this major stress drop is associated with formation of the initial gouge strand it may seem surprising that subsequent strands (microscopically so similar) have such different stress signatures. However, the first strand simply needs to be less stiff than the intact matrix, which is highly likely, for this to be understood.

We now present a conceptual model (Mair, 1997) consistent with our laboratory observations to describe the progressive evolution of a zone of deformation bands with increasing strain. [1] Microcracking associated with the strain hardening observed in the macroscopic loading curve occurs prior to failure. [2] Macroscopic shear failure of sample along a plane occurs by an increase in differential stress and a decrease in sample cohesion due to the microfracturing. [3] Strain is accommodated by frictional sliding along the new shear zone (strand). [4] This initial strand then loads the surrounding area elastically. The stress field induced is assumed to be consistent with elastic crack models (e.g. Kostrov and Das, 1982; after Das and Scholz, 1981) which predict a reduction in stress on the strand itself and in the region immediately adjacent but a significant increase in stress in regions parallel to the original strand and a finite distance away. [5] These new regions may be weakened by induced microcracking (Teufel, 1981) which can be considered both a 'wake' of damage related to the initial strand, and the 'process zone' of the next strand. [6] At this stage, the frictional strength of the initial gouge strand may have increased while the stress on it has decreased making continued displacement difficult. In contrast, stress is locally enhanced in new regions which have been mechanically weakened and hence are closer to failure. [7] At a certain point it becomes energetically favourable to accommodate additional deformation by initiating a new fault strand in this weakened new region rather than slip on the existing initial strand. The second strand, which will now be sliding frictionally, may then load the surrounding area similarly leading to additional strand formation.

We should note that the model hinges on local strain hardening of individual bands which, although seeming rather likely, has not been directly observed. The geometry of the sample and the resistance of the jacket may boost the likelihood of deformation switching to a new strand, rather than continuing slip on an existing strand, however, we believe it much more likely that the confining pressure of 34.5 MPa is influencing the style of deformation. In this weakly cemented sandstone it is inducing pseudo-cataclastic flow.

This model can account for the mechanism by which deformation shifts from one strand to another; why no strain hardening is observed in the macroscopic stress–strain curves simultaneously with band formation; the observed separation of parallel strands by a finite distance; and microcracking, pervasive in the fault zone pods, which can be a combination of process zone and wake damage.

4.3. The implications of deformation structures on fluid flow

One of the main applications of this study is the influence of these deformation structures on the flow of fluids and contaminants. Although permeability was not measured directly, microstructural observations highlight several features which may significantly affect fluid flow in a deformed sample. Gouge strands are expected to inhibit fluid migration due to reduced grain size and sorting. The strong correlation we find between number of strands and applied strain suggests that if each gouge strand reduces permeability by a comparable amount, then permeability may be influenced by applied strain. Axially orientated microcracks, prevalent in fault zone pods, introduce a new secondary porosity. Assuming these fractures are open (reasonable due to their epoxy impregnation) they may preferentially enhance permeability in the axial direction. These fault zone pods are longitudinally continuous and bounded laterally by less permeable gouge strands, hence can be envisaged as a series of high permeability pipes with little communication of fluids between them. The juxtaposition of 'high' and 'low' permeability structures affords the possibility of enhanced flow parallel to the fault zone and significantly reduced permeability perpendicular to the fault zone.

5. Conclusions

We have shown that zones of deformation bands form in highly porous sandstone under laboratory

Table 3
Stiffness calculations

Expt	Rig stretch (mm)	Uncorrected for rig stiffness		Corrected for rig stiffness	
		$\varepsilon_{\text{at failure}}$ (%)	$\varepsilon_{\text{total}}$ (%)	$\varepsilon_{\text{at failure}}$ (%)	$\varepsilon_{\text{total}}$ (%)
R5	0.895	1.77	4.22	1.30	3.75
R1	0.910	2.03	6.34	1.59	5.89
R6*	0.858	1.62	6.50	1.17	6.05
R3	0.866	1.92	9.16	1.47	8.71
R14	0.933	1.50	1.75	1.09	1.34
R12	0.999	1.58	2.0	1.14	1.56
R15	0.977	1.66	3.0	1.23	2.57
R16	0.992	1.50	8.0	1.07	7.56
R2	0.992	1.73	11.2	1.25	10.71

triaxial compression. The internal structure of the laboratory faults we have produced is similar to that of field examples of deformation bands. These zones consist of sets of individual granulated strands which interweave in planes perpendicular to maximum stress and lie sub-parallel at 030° to maximum stress in longitudinal planes. Skeletal pore space is significantly reduced within the bands and is reduced in the pods of host rock caught up between the bands. Extensive microfracturing in these fault zone pods adjacent to the bands has dominant orientation sub-parallel to maximum stress and may in fact enhance permeability in this direction. The number of strands is strongly positively correlated to amount of axial strain applied to the ends of the sample. The mean grain size in the strands, reduced with respect to the host rock, is similar for strands from samples shortened by different amounts. This implies that each strand accommodates only a finite amount of displacement. Although a strain hardening mechanism of formation would be interpreted from the structural data, the stress–strain curves show no macroscopic hardening post failure. We introduce a conceptual model for the structural evolution of zones of deformation bands which is entirely consistent with the laboratory observations. We propose that the initial band to form sets up a stress field which loads elements near but not adjacent to itself, weakening them and bringing them nearer to failure whilst the initial strand locks up due to increased friction. This offers a mechanism by which deformation can swap to a new strand rather than continue slip on the existing one without requiring macroscopic strain hardening.

Acknowledgements

K. Mair was supported by a NERC studentship. We thank P. Cowie and B. Ngwenya for many stimulating discussions regarding this work. We are grateful to A. Jackson and E. Scholz for technical support and O. Kwon for carrying out stiffness calibrations. Thanks are also extended to Baird and Stevenson Ltd, Locharbriggs, Scotland for providing fresh quarry rock samples and D. McCann, S. Horsman, M. Rotter and the University Grants Council who helped commission the deformation apparatus. We gratefully acknowledge the support of C. Marone and we thank J. Hadizadeh and an anonymous reviewer for thoughtful comments which improved this manuscript.

Appendix

The finite stiffness of the apparatus was determined by deforming steel and aluminium samples and monitoring the rig stretch as a function of axial load (Ohmyoung Kwon, personal communication, 1999). The stiffness was calculated as 1.05×10^9 N/m (or 9.0×10^{-4} mm/kN). We used this value along with the load at failure to calculate the apparatus deformation (rig stretch) for each individual experiment. Results are presented in the second column of Table 3. Accordingly we applied a stiffness correction to remove the effects of this rig deformation from the axial strain as shown in Table 3. Note that strain values quoted in the main text are uncorrected values.

References

Antonellini, M.A., Aydin, A., Pollard, D.D., 1994. Microstructure of deformation bands in porous sandstones at Arches National Park, Utah. Journal of Structural Geology 16, 941–959.

Aydin, A., Johnson, A.M., 1978. Development of faults as zones of deformation bands and slip surfaces in sandstone. Pure and Applied Geophysics 116, 931–942.

Aydin, A., Johnson, A.M., 1983. Analysis of faulting in porous sandstones. Journal of Structural Geology 5, 19–31.

Aydin, A., 1978. Small faults formed as deformation bands in sandstone. Pure and Applied Geophysics 116, 913–930.

Bernabe, Y., Brace, W.F., 1990. Deformation and fracture of Berea sandstone. In: Duba, A.G., Durham, W.B., Handin, J.W., Wang, H.F. (Eds.), The Brittle–Ductile Transition in Rocks. American Geophysical Union Monograph 56, pp. 91–101.

Biegel, R.L., Sammis, C.G., Dieterich, J.H., 1989. The frictional properties of a simulated gouge having a fractal particle distribution. Journal of Structural Geology 11, 827–846.

Das, S., Scholz, C.H., 1981. Off-fault aftershocks caused by shear stress increase? . Bulletin of the Seismological Society of America 71, 1669–1675.

Dunn, D.E., LaFountain, L.J., Jackson, R.E., 1973. Porosity dependence and mechanisms of brittle fracture in sandstones. Journal of Geophysical Research 78, 2403–2417.

Engelder, J.T., 1974. Cataclasis and the generation of fault gouge. Geological Society of America Bulletin 85, 1515–1522.

Fowles, J., Burley, S., 1994. Textural and permeability characteristics of faulted, high porosity sandstones. Marine and Petroleum Geology 11, 608–623.

Friedman, M., Logan, J.M., 1970. Microscopic feather fractures. Geological Society of America Bulletin 81, 3417–3420.

Friedman, M., Logan, J.M., 1973. Luders bands in experimentally deformed sandstone and limestone. Geological Society of America Bulletin 84, 1465–1476.

Gu, Y., Wong, T.F., 1994. Development of shear localisation in simulated quartz gouge: Effects of cumulative slip and gouge particle size. Pure and Applied Geophysics 143, 387–423.

Hirth, G., Tullis, J., 1989. The effects of pressure and porosity on the micromechanics of the brittle–ductile transition in quartzite. Journal of Geophysical Research 94, 17825–17838.

Jaeger, J.C., Cook, N.G.W., 1979. Fundamentals of Rock Mechanics, 3rd edn. Halsted Press, New York.

Jamison, W.R., Stearns, D.W., 1982. Tectonic deformation of the Wingate sandstone, Colorado National Monument. American Association of Petroleum Geologists Bulletin 66, 2584–2608.

Kostrov, B., Das, S., 1982. See Kostrov, B., Das, S., 1988. Principles of Earthquake Source Mechanics. Cambridge University Press, Cambridge.

Lockner, D.A., Byerlee, J.D., Kuksenko, V., Ponomarev, A., Sidorin, A., 1991. Quasi-static fault growth and shear fracture energy in granite. Nature 350, 39–42.

Mair, K., 1997. Experimental studies of fault zone development in a porous sandstone. PhD thesis, University of Edinburgh.

Marone, C., Scholz, C.H., 1989. Particle size distribution and microstructures within simulated fault gouge. Journal of Structural Geology 11, 799–814.

Menendez, B., Zhu, W., Wong, T.-F., 1996. Micromechanics of brittle faulting and cataclastic flow in Berea Sandstone. Journal of Structural Geology 18, 1–16.

Paterson, M.S., 1978. Experimental Rock Deformation—the Brittle Field. Springer-Verlag, Berlin.

Pittman, E.D., 1981. Effect of fault related granulation on porosity and permeability of quartz sandstones, Simpson Group (Ordovician), Oklahoma. American Association of Petroleum Geologists Bulletin 65, 2381–2387.

Rice, J.R., 1992. Fault stress state, pore pressure distributions, and the weakness of the San Andreas Fault. In: Evans, B., Wong, T.-F. (Eds.), Fault Mechanics and Transport Properties of Rock. Academic Press, London, pp. 475–503.

Rudnicki, J.W., Rice, J.R., 1975. Theory of inelastic deformation for strain hardening (or softening) materials. Journal of the Mechanics and Physics of Solids 23, 371–394.

Sammis, C.G., King, G., Biegel, R., 1987. The kinematics of gouge deformation. Pure and Applied Geophysics 125, 777–812.

Scott, D.R., Marone, C.J., Sammis, C.G., 1994. The apparent friction of granular fault gouge in sheared layers. Journal of Geophysical Research 99, 7231–7246.

Teufel, L.W., 1981. Pore volume changes during frictional sliding of simulated faults. In: Mechanical Behaviour of Crustal Rocks: the Handin Volume. American Geophysical Union Monograph 24, pp. 135–145.

Underhill, J.R., Woodcock, N.H., 1987. Faulting mechanisms in high porosity sandstones; New Red Sandstone, Arran, Scotland. In: Jones, M.E., Preston, R.M.F. (Eds.), Deformation of Sediments and Sedimentary Rocks. Geological Society of London Special Publication 29, pp. 91–105.

Weeks, J.D., 1980. Some aspects of frictional sliding at high normal stress. PhD thesis, Stanford University, California.

Wong, T.-F., David, C., Zhu, W., 1997. The transition from brittle faulting to cataclastic flow in porous sandstones: Mechanical deformation. Journal of Geophysical Research 102, 3009–3025.